Research Square

Preprints are preliminary reports that have not undergone peer review.
They should not be considered conclusive, used to inform clinical practice,
or referenced by the media as validated information.

# Photocatalytic Performance of Ce, N-Doped Cu2SO3·CuSO3·2H2O Supported on Hollow Ceramic Microspheres

**Guodong Hao**
Mudanjiang Normal University
**Haoyan Guo**
Mudanjiang Normal University
**Haoxuan Sun**
theshx@163.com

Yantai Nanshan University

**Research Article**

**Keywords:** Cu2SO3, CuSO3, 2H2O Ce N-doping Photocatalysis Ceramic hollow microspheres First principle

**Posted Date:** November 5th, 2026

**DOI:** https://doi.org/10.21203/rs.3.rs-11357681/v1

**License:** This work is licensed under a Creative Commons Attribution 4.0 International License.
Read Full License

**Additional Declarations:** No competing interests reported.

# Photocatalytic Performance of Ce, N-Doped $Cu_2SO_3 \cdot CuSO_3 \cdot 2H_2O$ Supported on Hollow Ceramic Microspheres

Guodong Hao[1], Haoyan Guo[1], Haoxuan Sun[2*]

[1]College of Chemistry and Chemical Engineering, Mudanjiang Normal University, Mudanjiang 157011, China.
[2]College of Chemical Engineering and Technology, Yantai Nanshan University, Yantai 265713, China.

*Corresponding author(s). E-mail(s): theshx@163.com;

**Abstract**

$Cu_2SO_3 \cdot CuSO_3 \cdot 2H_2O$-based photocatalysts doped with Ce and N were syn- thesized via a liquid-phase method and further supported on ceramic hollow microspheres (CHMBs) to enhance their visible-light photocatalytic perfor- mance. The as-prepared materials were characterized by scanning electron microscopy (SEM), X-ray diffraction (XRD), Raman spectroscopy, X-ray photo- electron spectroscopy (XPS), UV-Vis diffuse reflectance spectroscopy (DRS), and photoluminescence (PL) spectroscopy. The photocatalytic activities were evalu- ated under xenon lamp irradiation. The doping mechanisms were investigated via first-principles calculations. The results indicated that the optimal molar ratios of Ce and N were 1.5% and 2.0%, respectively, under which the degrada- tion rates of methyl orange reached 87% and 85%, respectively. Upon loading onto CHMB, the degradation rates further increased to 98% and 97%, and the catalytic efficiency remained at 82% after four recycling tests. First-principles calculations revealed that Ce doping reduced the band gap from 3.464 eV to 1.660 eV, thereby facilitating the separation and migration of photogenerated charge carriers. The synergistic effect of Ce/N co-doping and the CHMB support significantly improved the photocatalytic activity of $Cu_2SO_3 \cdot CuSO_3 \cdot 2H_2O$.

**Keywords:** $Cu_2SO_3 \cdot CuSO_3 \cdot 2H_2O$ Ce N-doping Photocatalysis Ceramic hollow microspheres First principle

# 1 Introduction:

Photocatalytic technology is considered one of the key approaches for green environmental remediation, as it enables the utilization of solar energy to drive catalytic reactions that mineralize organic pollutants into harmless small molecules, offering advantages such as mild reaction conditions, no secondary pollution, and good recy- clability [1–6]. Nevertheless, its practical application is still limited by several intrinsic limitations, including rapid recombination of photogenerated electron-hole pairs, a nar- row visible-light response, and insufficient active sites, which collectively hinder further improvement in photocatalytic performance. Elemental doping has been recognized as an effective strategy to modulate the electronic structure, enhance the charge carrier separation efficiency, and optimize the crystal structure of photocatalysts[7–10]. Therefore, the development of novel photocatalytic materials with high catalytic activity, robust stability, and favorable reusability has become an important research direction in the field of environmental catalysis [11]. $Cu_2SO_3{\cdot}CuSO_3{\cdot}2H_2O$, an emerging copper-based functional material, has attracted considerable attention in the degradation of organic pollutants because of its abundant raw material sources, simple preparation process, and promising photocatalytic potential [12, 13].

Rare-earth element doping has been widely employed in the modification of photocatalytic materials owing to its ability to introduce defect levels, regulate electronic structures, and promote photogenerated charge carrier migration. Among these elements, Ce exhibits reversible $Ce^{3+}/Ce^{4+}$ valence switching and excellent electron storage capability, which effectively facilitates electron transfer and suppresses carrier recombination[14, 15]. Moreover, nonmetal N doping can further modulate the local electronic environment of the material, enhance the light absorption performance, and improve the separation efficiency of photogenerated charge carriers [16], Similar nonmetal-doping effects have also been rationalized by theoretical studies [17]. In addition, immobilizing catalysts onto the surface of ceramic hollow microspheres not only improves catalyst dispersion and stability but also effectively prevents nanoparticle agglomeration and enhances the recyclability of the material[18, 19]. To date, studies on the synergistic Ce and N codoping of $Cu_2SO_3{\cdot}CuSO_3{\cdot}2H_2O$ are scarce, and the underlying mechanisms governing the synergistic modulation of the crystal structure, electronic structure, and photocatalytic performance are still unclear. Moreover, systematic investigations into the effects of ceramic hollow microspheres as supports on catalyst dispersion, interfacial bonding, and cycling stability are lacking. Therefore, the preparation of Ce and N synergistically codoped supported $Cu_2SO_3{\cdot}CuSO_3{\cdot}2H_2O$ composite photocatalytic materials, combined with theoretical calculations to gain in-depth insight into the structure-activity relationship and performance enhancement mechanisms, is highly important for research.

Methyl orange (MO) was employed as a model pollutant to evaluate the photocatalytic degradation performance under simulated solar irradiation. First-principles calculations were further performed to investigate the band structure and density of states of Ce-doped $Cu_2SO_3{\cdot}CuSO_3{\cdot}2H_2O$. Through a combination of experimental characterization and theoretical computation, the underlying mechanisms responsible for the enhanced photocatalytic activity were elucidated, particularly regarding the synergistic effects of Ce and N codoping, as well as the support of ceramic hollow microspheres. To the best of our knowledge, there have been no prior reports on

Ce- and N-doped $Cu_2SO_3 \cdot CuSO_3 \cdot 2H_2O$ combined with first-principles studies, either domestically or internationally, which constitutes the innovative aspect of this work.

# 2 Experimental Section:

## 2.1 Preparation of Ce- and N-doped $Cu_3(SO_3)_2(H_2O)_2$ Photocatalysts

In a typical synthesis, 152 mL of 0.3 mol/L $CuSO_4 \cdot 5H_2O$ solution was transferred into a beaker (solution A). Meanwhile, 152 mL of 0.3 mol/L $Na_2SO_3$ solution and 40 mL of HAc-NaAc buffer (pH = 6) were mixed in another beaker (solution B). Both solutions were separately placed in an 80 ˚C water bath and stirred for 30 min, during which solution B was kept sealed. Subsequently, solution B was rapidly poured into solution A, and the mixture was continuously stirred under sealed conditions in a water bath for another 20 min, yielding a brick-red precipitate. After aging for 40 min, the mixture was again sealed, stirred, and heated for 20 min, followed by another 40 min aging step. This procedure was repeated three times. The resulting precipitate was collected by suction filtration and dried in an oven at 80 ˚C for 4 h to obtain the powdered $Cu_2SO_3 \cdot CuSO_3 \cdot 2H_2O$ product.

The preparation procedure for the modified $Cu_2SO_3 \cdot CuSO_3 \cdot 2H_2O$ sample was essentially the same as that for the pristine powder sample. For Ce-doped $Cu_2SO_3 \cdot CuSO_3 \cdot 2H_2O$, cerium nitrate was introduced into solution A during synthesis, with nominal Ce/Cu molar ratios of 0.5%, 1.0%, 1.5%, 2.0%, and 2.5%. For N-doped $Cu_2SO_3 \cdot CuSO_3 \cdot 2H_2O$, urea was added to solution A instead, with the same nominal molar ratios of 0.5%, 1.0%, 1.5%, 2.0%, and 2.5%.

For the preparation of the $Cu_2SO_3 \cdot CuSO_3 \cdot 2H_2O$ catalyst supported on ceramic hollow microspheres, the ceramic hollow microspheres were first added to solution A prior to mixing with solution B. The two solutions were then mixed under mechanical stirring, followed by intermittent stirring after combination.

## 2.2 Photocatalytic activity measurements

A 100 mL aliquot of methyl orange (MO) solution with a concentration of 10 mg/L was used as the model pollutant and placed in a double-walled beaker equipped with a circulating cooling system, through which cooling water was continuously circulated. Photocatalytic degradation experiments were carried out by adding 0.2 g of powder catalyst or 1.155 g of supported catalyst (with a loading amount of 17.31%). A 300 W xenon lamp was employed as the simulated solar light source, and the solution was positioned at a distance of 25 cm directly below the lamp. At 15 min intervals, approximately 4 mL of the suspension was sampled and centrifuged at 5200 rpm for 10 min. The supernatant was then collected for absorbance measurement. The degradation efficiency was calculated according to the following equation:

$$Degradationrate = (A_0 - A)/A_0 * 100\%$$

where $A_0$is the initial absorbance of the pollutant before photocatalytic degradation and A is the absorption after photocatalytic degradation.

### 2.3 Computational models and methods

As shown in Fig. 1(a), the crystal structure of $Cu_2SO_3 \cdot CuSO_3 \cdot 2H_2O$ is composed of tetrahedral [$Cu^{I}O_3S$], trigonal pyramidal [$SO_3$], and [$Cu^{II}O_4(H_2O)_2$] units. It crystallizes in a monoclinic system (a = b = c, $\alpha = \gamma = 90^\circ$, $\beta \neq 90^\circ$) with space group $P2_1/c$. The lattice parameters of $Cu_2SO_3 \cdot CuSO_3 \cdot 2H_2O$ are a = 5.5671 Å, b = 7.7875 Å, c = 8.3635 Å, $\alpha = \gamma = 90^\circ$, and $\beta = 91.279^\circ$. The structural model after substituting one Cu with Ce is depicted in Fig. 1 (b), with refined lattice constants of a = 5.6868 Å, b = 8.3803 Å, c = 8.7107 Å, $\alpha = 90^\circ$, $\beta = 91.924^\circ$, and $\gamma = 89.099^\circ$. First-principles calculations were performed via the plane-wave ultrasoft pseudopotential method within the generalized gradient approximation (GGA+U) framework based on the PBE functional [20]. A plane-wave cutoff energy of 550 eV was adopted, and the convergence criterion for total energy was set to $1 \times 10^{-5}$ eV/atom. The Brillouin zone was sampled with a $6 \times 4 \times 4$ k-point mesh, and the force on each atom converged to less than 0.02 eV/atom.

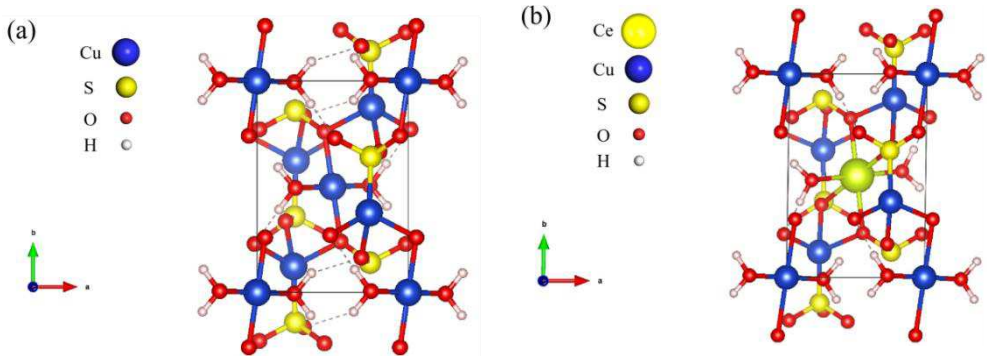



**Fig. 1**: Model before and after Ce doping

## 3 Results and Discussion

### 3.1 Surface morphology and elemental distribution (SEM)

Fig. 2 presents the scanning electron microscopy (SEM) morphologies and elemental mapping results of the different catalysts. As shown in Fig. 2 (a), pristine $Cu_2SO_3 \cdot CuSO_3 \cdot 2H_2O$ has a regular core-shell structure, with the surface constructed from accumulated octahedral crystalline units, indicating a high degree of structural integrity. This unique geometric morphology is likely attributed to the anisotropic crystal growth induced by the coordination of $SO^{2-}$ ligands, which promotes pref- erential growth along specific crystallographic planes, thereby forming a well-defined octahedral architecture.

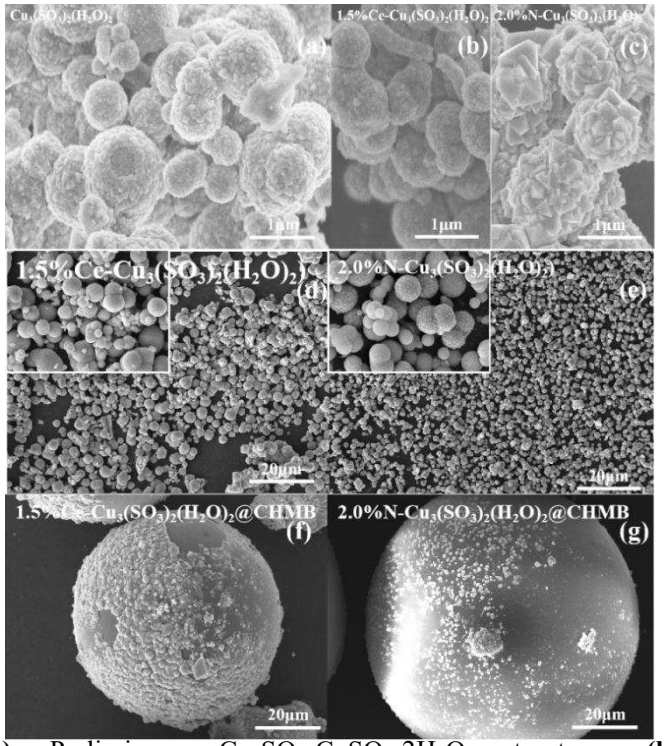



**Fig. 2**: **(a)** Preliminary $Cu_2SO_3 \cdot CuSO_3 \cdot 2H_2O$ structure; **(b)** Ce-doped $Cu_2SO_3 \cdot CuSO_3 \cdot 2H_2O$ structure; **(c)** N-doped $Cu_2SO_3 \cdot CuSO_3 \cdot 2H_2O$ structure; **(d)** SEM image of Ce-doped $Cu_2SO_3 \cdot CuSO_3 \cdot 2H_2O$ at 2000× magnification; **(e)** SEM image of N-doped $Cu_2SO_3 \cdot CuSO_3 \cdot 2H_2O$ at 2000× magnification; **(f)** Elemental mapping of 1.5% Ce-doped $Cu_2SO_3 \cdot CuSO_3 \cdot 2H_2O$; **(g)** Elemental mapping of 2.0% N-doped $Cu_2SO_3 \cdot CuSO_3 \cdot 2H_2O$.

Upon Ce doping (Fig. 2 (b)), the catalyst retained a spherical aggregated morphology; however, the size of the octahedral grains constituting the spheres was markedly reduced, and the surface became smoother and denser. This observation suggests that the introduction of $Ce^{3+}$ significantly regulates the crystal growth process. Given that the ionic radius of $Ce^{3+}$(1.02 Å) is considerably larger than that of $Cu^{2+}$(0.73 Å), the partial incorporation of $Ce^{3+}$ into the lattice induces local lattice distortion, thereby weakening the preferential growth along the dominant crystallographic planes and limiting further grain growth, ultimately resulting in a more uniform and compact aggregate.

In contrast, the N-doped sample (Fig. 2 (c)) exhibited more pronounced morphological reconstruction. The original regular octahedra gradually transformed into a flower-like cluster structure with sharp edges, indicating that the introduction of N altered the nucleation and growth mechanisms. It is speculated that the abun- dant defect sites generated by N doping may serve as new nucleation centers,

thereby increasing the nucleation rate and modifying the crystal growth kinetics, ultimately leading to the formation of smaller and more loosely arranged polycrystalline aggregates.

To further compare the influence of the two doping strategies on the microstructure, SEM images of the Ce-doped and N-doped samples at 2000× magnification are shown in Fig. 2 (d) and (e), respectively. The polycrystalline aggregates formed by N doping are substantially smaller than those of the Ce-doped sample, suggesting that N doping is more effective in grain refinement. This result is consistent with the grain size variations derived from subsequent XRD analysis.

To improve the recyclability of the catalyst, the samples were further loaded onto the surface of ceramic hollow microspheres (CHMBs), as depicted in Fig. 2 (f) and (g). The Ce-doped sample was uniformly coated on the CHMB surface in the form of relatively large aggregates, whereas the N-doped sample, despite a slightly lower overall loading, exhibited a more homogeneous distribution of catalyst particles. This discrepancy indicates that the two doping approaches exert distinct effects on the deposition behavior of the catalyst onto the support.

## 3.2 X-ray Diffraction Analysis (XRD)

To further elucidate the underlying mechanisms by which Ce doping, N doping, and CHMB loading affect the photocatalytic performance of $Cu_2SO_3 \cdot CuSO_3 \cdot 2H_2O$, XRD measurements were performed on the samples, and the results are presented in Fig. 3. As shown in Fig. 3 (a) and (b), the diffraction peaks of the pristine $Cu_2SO_3 \cdot CuSO_3 \cdot 2H_2O$ sample are in good agreement with the standard PDF card (PDF No. 19–0408), corresponding to the monoclinic phase of $Cu_2SO_3 \cdot CuSO_3 \cdot 2H_2O$ with space group $P2_1/c$, indicating that the as-prepared sample possesses good crystallinity. After Ce and N doping, all the samples retained the main crystalline phase of $Cu_2SO_3 \cdot CuSO_3 \cdot 2H_2O$ without the appearance of additional impurity peaks, suggesting that the doping did not disrupt the crystal structure but rather primarily influenced the microscopic crystal growth process.

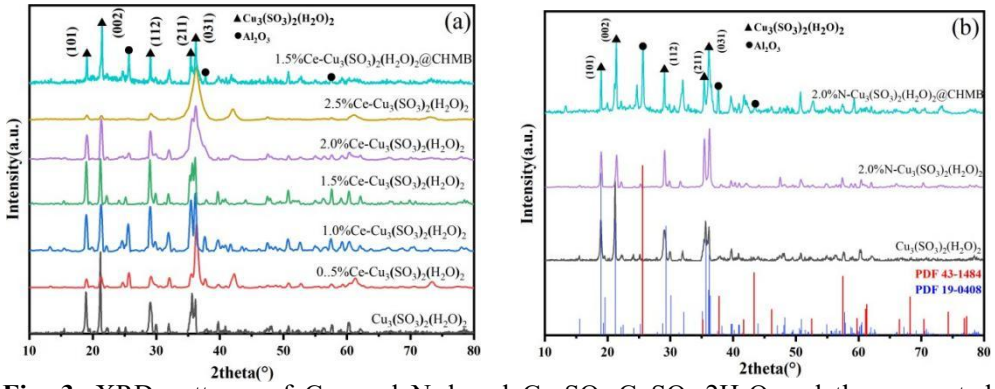



**Fig. 3**: XRD patterns of Ce- and N-doped $Cu_2SO_3 \cdot CuSO_3 \cdot 2H_2O$ and the supported catalysts.

As depicted in Fig. 3 (a), when the Ce doping amount was increased to 2.0%, the two diffraction peaks located at approximately 35.6° and 36.2° gradually merged into a broad peak, indicating a reduction in the grain size. This can be attributed mainly to the fact that a higher concentration of Ce doping provides more nucleation sites, thereby increasing the nucleation rate and suppressing further grain growth. As shown in Fig. 3 (b), N doping similarly did not alter the main crystalline phase of the material but modulated only the grain size and crystal growth mode.

For the CHMB-loaded samples, diffraction peaks corresponding to $Al_2O_3$(PDF No. 43–1484) were observed, which are characteristic of the ceramic hollow microsphere support, further confirming that $Cu_2SO_3 \cdot CuSO_3 \cdot 2H_2O$ is predominantly dispersed on the CHMB surface in the loaded state.

## 3.3 Raman Spectra Analysis

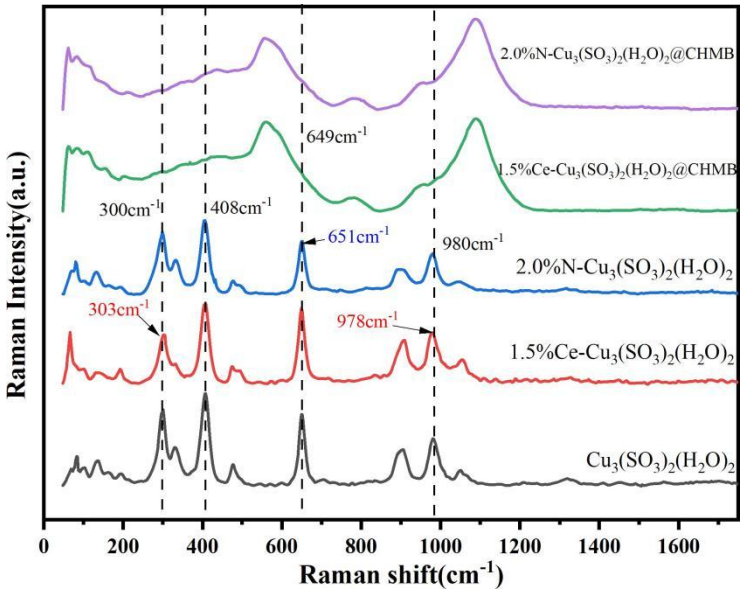



**Fig. 4**: Raman spectra of Ceand N-doped $Cu_2SO_3 \cdot CuSO_3 \cdot 2H_2O$ and the supported catalysts.

To analyze the local lattice changes induced by doping, Raman spectroscopy was performed on the samples. As shown in Fig. 4, the pristine sample exhibited a Cu-O bond bending vibration peak at approximately 300 $cm^{-1}$. After 1.5% Ce doping, this peak shifted from 300 $cm^{-1}$ to 303 $cm^{-1}$. This shift is attributed mainly to the fact that the ionic radius of $Ce^{3+}$ is larger than that of $Cu^{2+}$; the partial substitution of Cu sites by $Ce^{3+}$ induces local lattice expansion, which alters the Cu-O bond length and bond angle, thereby modifying the vibrational environment of the Cu-O bond. Concurrently, the $\nu_1$ symmetric stretching vibration peak of $SO_3^{2-}$ near 980 $cm^{-1}$ also

exhibited a slight shift, indicating that Ce doping reduces the local lattice symmetry and changes the coordination environment of $SO_3^{2-}$. For the N-doped sample, the vibration peak near 649 $cm^{-1}$ shifted to 651 $cm^{-1}$ with a concomitant decrease in intensity, which may be associated with the formation of S-N bonds upon N doping and the resulting increase in local bond stiffness.

Compared with those of the powder samples, all the Raman peaks of the CHMB-loaded samples exhibited a certain degree of broadening. This is mainly attributable to the restricted continuous grain growth during the catalyst loading process, which led to the formation of partially amorphous regions, accompanied by an increase in structural defects such as oxygen vacancies, thereby resulting in increased lattice disorder. An appropriate number of defects can serve as electron trapping centers, providing favorable conditions for the separation and migration of photogenerated charge carriers and thus contributing to improved photocatalytic performance.

## 3.4 Optical Absorption Properties (UV–Vis DRS)

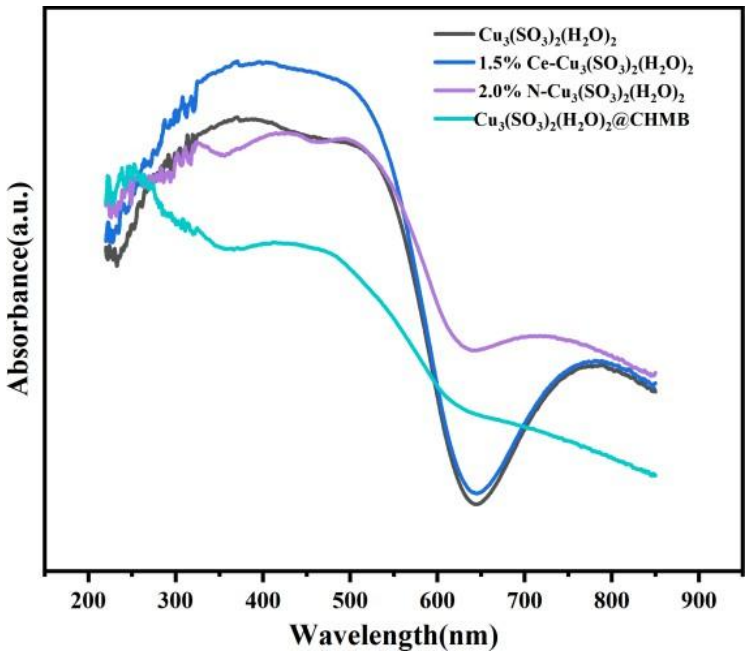



**Fig. 5**: UV–Vis DRS of Ce and N-doped $Cu_2SO_3 \cdot CuSO_3 \cdot 2H_2O$ and the supported catalysts.

Modifications in the crystal structure and local coordination environment further influence the optical properties of the material. As shown in Fig. 5, pristine $Cu_2SO_3 \cdot CuSO_3 \cdot 2H_2O$ exhibited moderate absorption in both the ultraviolet and visible regions. Upon Ce doping, a significant broadening of the absorption band is

observed in the range of 300-550 nm, indicating enhanced absorption intensity in both the UV and visible regions, accompanied by a redshift of the absorption edge, which suggests that the photoresponse range of the material has been extended. This indicates that Ce doping alters the electronic structure of the material, leading to a reduction in the band gap and thereby enabling the absorption of more low-energy visible light. In contrast, the N-doped sample exhibited a more pronounced redshift in the visible region, along with a further increase in the absorption peak intensity, suggesting that N doping is more favorable for improving the utilization efficiency of visible light. For the CHMB-loaded samples, a notably higher absorption intensity is observed across the entire measured wavelength range, indicating that the support not only improves the dispersion state of the catalyst but also enhances the light-harvesting capability of the material, thereby creating favorable conditions for the generation of additional photogenerated charge carriers.

## 3.5 Photoluminescence spectroscopy (PL) analysis

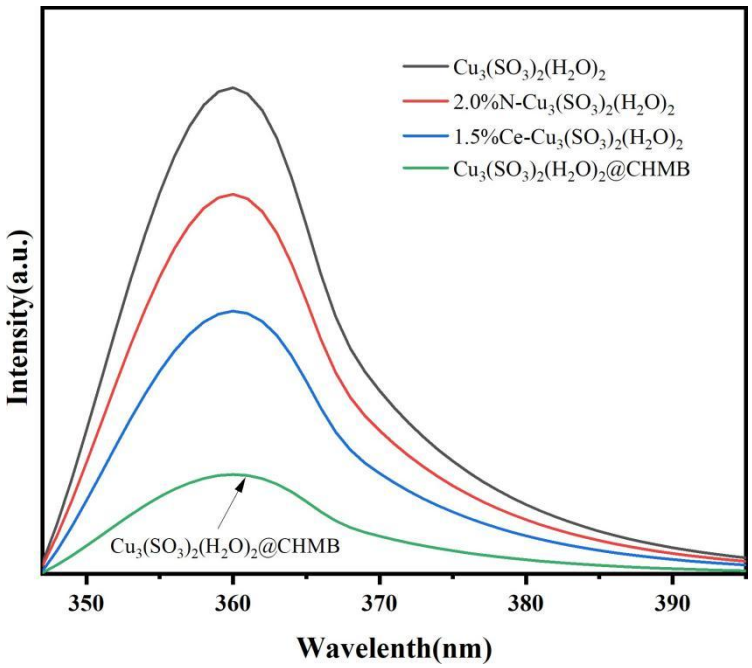



**Fig. 6**: Fluorescence spectra of Ce, N-doped $Cu_2SO_3 \cdot CuSO_3 \cdot 2H_2O$ and the supported catalysts.

A strong light absorption ability alone does not fully determine the photocatalytic performance of a material; the separation efficiency of photogenerated electrons and holes is equally crucial. Therefore, PL measurements were conducted on the samples. As shown in Fig. 6, in the range of 350-370 nm, the PL intensities of both the Ce-doped

and N-doped samples are significantly lower than that of the pristine sample, indicating that both doping strategies facilitate the separation of photogenerated charge carriers. Among them, the Ce-doped sample exhibited the lowest PL intensity, suggesting that its electron-hole recombination rate was further suppressed. This is mainly attributed to the fact that the defect levels introduced by Ce doping can effectively trap electrons, whereas a moderate grain size reduces grain boundary recombination and enhances carrier migration efficiency. In contrast, although N doping significantly enhances the visible-light absorption of the material, further grain refinement introduces more grain boundaries and defects, some of which may act as electron-hole recombination centers. As a result, the PL intensity of the N-doped sample is lightly greater than that of the Ce-doped sample, which also explains why the photocatalytic performance of the N-doped sample is slightly inferior to that of its Ce-doped counterpart. Notably, the CHMB-loaded sample has the lowest PL emission intensity, indicating that CHMB can serve as an electron transport platform, facilitating the rapid migration of photogenerated electrons and shortening the carrier diffusion pathway, thereby suppressing electron-hole recombination to the greatest extent.

## 3.6 X-ray photoelectron spectroscopy (XPS)

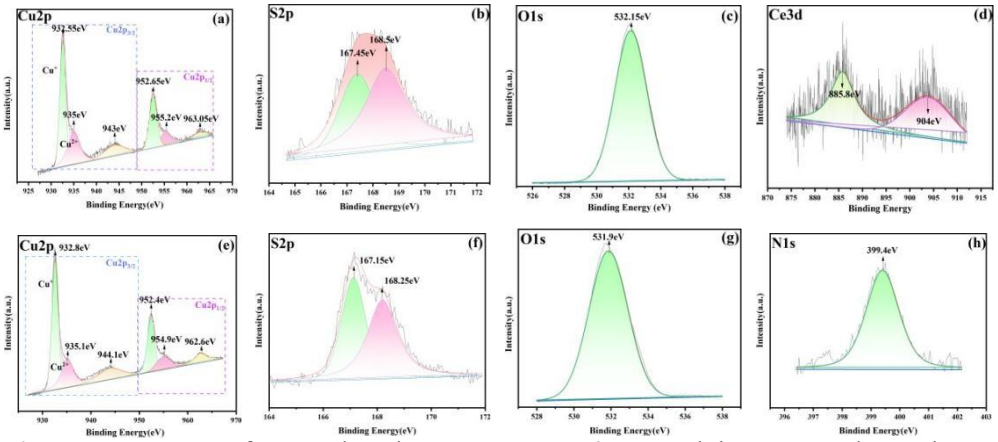



**Fig. 7**: XPS spectra of Ce, N-doped $Cu_2SO_3 \cdot CuSO_3 \cdot 2H_2O$ and the supported cata- lysts.

Fig. 7 presents the X-ray photoelectron spectroscopy (XPS) spectra of Ce- and N-doped $Cu_2SO_3 \cdot CuSO_3 \cdot 2H_2O$@CHMB. As shown in Fig. 7 (a), the Cu 2p core- level spectrum of Ce-doped $Cu_2SO_3 \cdot CuSO_3 \cdot 2H_2O$@CHMB exhibited a narrow and symmetric peak at a binding energy of 932.55 eV, which was attributed to the $Cu^+$ species in Cu $2p_3/_2$, whereas the peak at 935 eV corresponded to $Cu^{2+}$. A satellite peak of $Cu^{2+}$ is observed at approximately 10 eV above the higher binding energy side. In the Cu $2p_1/_2$ region, the peaks for $Cu^+$ and $Cu^{2+}$ are located at 952.45 eV and 954.9 eV, respectively, with a satellite peak appearing at 963.05 eV. These

results indicate that the Cu in $Cu_2SO_3 \cdot CuSO_3 \cdot 2H_2O$ exists in two valence states. In Fig. 7 (b), the S 2p spectrum displays a doublet structure with binding energies of 167.45 eV and 168.5 eV, corresponding to an energy separation of 1.05 eV, which is characteristic of $SO_3^{2-}$ species. Fig. 7 (c) shows the O 1 s spectrum, which is attributed mainly to oxygen species from sulfite groups and crystalline water and partially to the formation of metal oxides during the doping process. Fig. 7 (d) presents the Ce 3d XPS spectrum, confirming the successful incorporation of Ce. Owing to the relatively low doping concentration, the spectrum exhibited a noisy fluctuation pattern. Figs. 7 (e)-(h) display the XPS spectra of N-doped $Cu_2SO_3 \cdot CuSO_3 \cdot 2H_2O$ @CHMB. The Cu 2p, S 2p, and O 1 s spectra are similar to those of their Ce-doped counterparts. As shown in Fig. 7 (h), the N 1 s spectrum confirms the presence of N, with a single characteristic peak located at 399.4 eV, suggesting that the incorporated N exists in a single chemical state, presumably as $-NH_2$.

## 3.7 DFT Calculations: Density of States and Band Structure Analysis (DFT)

Fig. 8(a) presents the density of states (DOS) for the unit cell model of $Cu_2SO_3 \cdot CuSO_3 \cdot 2H_2O$ before and after Ce doping. No significant difference is observed between the spin-up and spin-down states near the Fermi level, indicating that $Cu_2SO_3 \cdot CuSO_3 \cdot 2H_2O$ is a nonmagnetic material. 8(b) shows the partial density of states (PDOS) of the undoped sample, whereas Fig. 8(c) shows the PDOS after Ce doping. As shown in Fig. 8(b), prior to doping, the Cu-3d and O-2p orbitals exhibit pronounced peaks in the lower energy region, contributing substantially to the total DOS. The S-3p and S-3 s orbitals show a certain DOS distribution in specific energy ranges, although their overall contribution is relatively minor. After Ce doping, the overall DOS distribution remains similar to that of the undoped sample; however, an increase in the DOS near the Fermi level is observed, implying that electrons have a greater probability of transitioning to the conduction band in this energy region. This enhancement facilitates an increase in carrier concentration and mobility, thereby accelerating the separation and transport processes of photogenerated charge carriers.

Fig. 9(a) shows the band structure of $Cu_2SO_3 \cdot CuSO_3 \cdot 2H_2O$, from which a distinct energy gap between the valence band maximum (VBM) and the conduction band minimum (CBM) can be observed, with an Eg*Eg* of 3.464 eV. After Ce doping, as shown in Fig. 9(b), the band gap is significantly reduced, indicating that Ce doping markedly narrows the band gap of $Cu_2SO_3 \cdot CuSO_3 \cdot 2H_2O$, transforming it from a wide bandgap material into a narrow bandgap semiconductor. Concurrently, the band distribution near the Fermi level is modified. The reduction in lattice symmetry induced by Ce doping leads to a shift in the edges of both the conduction band (CB) and the valence band (VB); the calculated results show that both the CB and the VB shift downward. After Ce doping, the band gap decreases to 1.660 eV, and impurity levels emerge within the band gap. The reduction in the band gap, together with the generation of impurity levels, influences the optical absorption properties of the material by lowering the energy required for electrons to transition from the valence band to the conduction band, thereby increasing light absorption and facilitating the photocatalytic reaction.

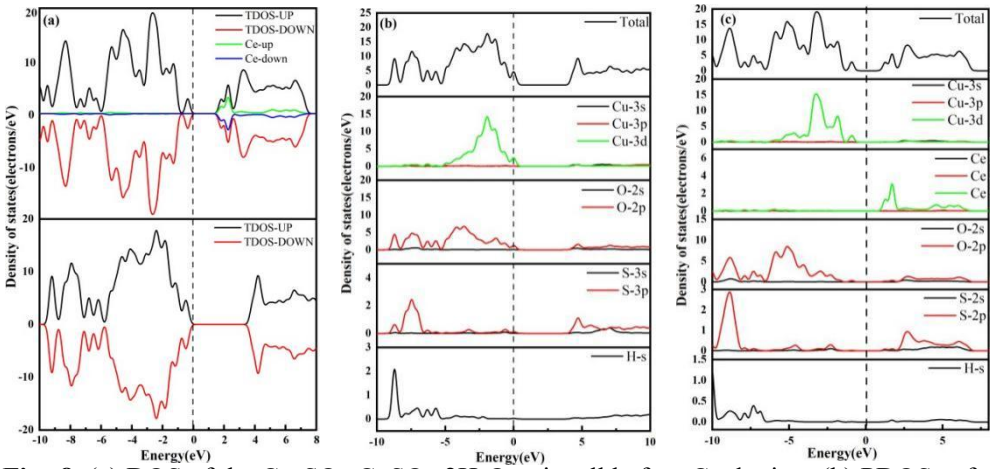



**Fig. 8**: (a) DOS of the $Cu_2SO_3 \cdot CuSO_3 \cdot 2H_2O$ unit cell before Ce doping; (b) PDOS of the undoped and (c) Ce-doped samples.

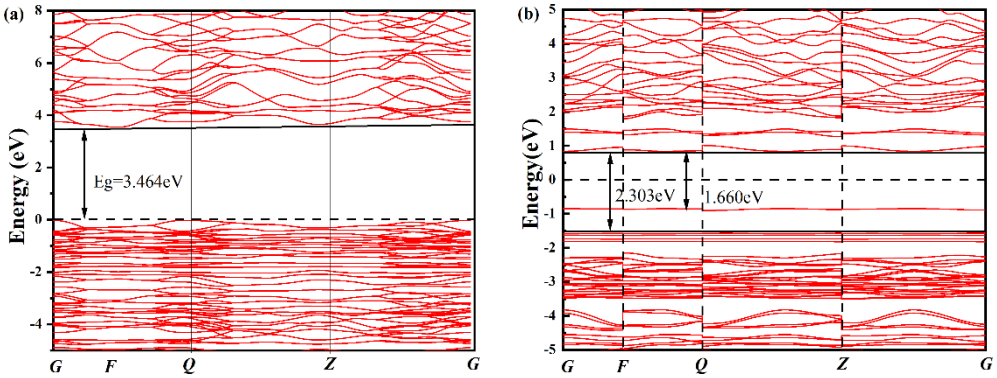



**Fig. 9**: Band structure diagrams of $Cu_2SO_3 \cdot CuSO_3 \cdot 2H_2O$ (a) before and (b) after Ce doping.

## 3.8 Photocatalytic Performance

To verify the influence of the aforementioned structural modifications on the photocatalytic performance of the materials, visible-light degradation experiments and cyclic stability tests were conducted using methyl orange (MO) as the model pollu- tant, and the results are presented in Fig. 10(a) shows the degradation rates of methyl orange over Ce- and N-doped $Cu_3(SO_3)_2(H_2O)_2$. After 1 h of illumination, pristine $Cu_2SO_3 \cdot CuSO_3 \cdot 2H_2O$ exhibited a degradation rate of 61%, which is consistent with its UV-vis diffuse reflectance behavior under visible light. When the Ce doping molar ratio reached 1.5%, the photocatalytic performance was enhanced to the greatest extent, achieving a degradation rate of 87% within 1 h. However, excessive doping resulted in only a moderate improvement in photocatalytic activity, which is in agreement with

the XRD analysis, indicating that overdoping may induce grain aggregation and the formation of charge carrier recombination centers. Thus, an optimal Ce doping molar ratio exists for enhancing the photocatalytic performance of $Cu_2SO_3 \cdot CuSO_3 \cdot 2H_2O$, which was determined to be 1.5% in this study. As shown in Fig. 10(b), for N doping, the optimal molar ratio was found to be 2.0%, yielding a degradation rate of 85% after 1 h of illumination, whereas the degradation rate decreased to 79% when the doping ratio was increased to 2.5%. Furthermore, after loading the optimally doped samples onto ceramic hollow microspheres (CHMBs), the degradation rates reached 98% and 97% for the Ce- and N-doped samples, respectively, indicating that the CHMB support can further enhance the photocatalytic performance.

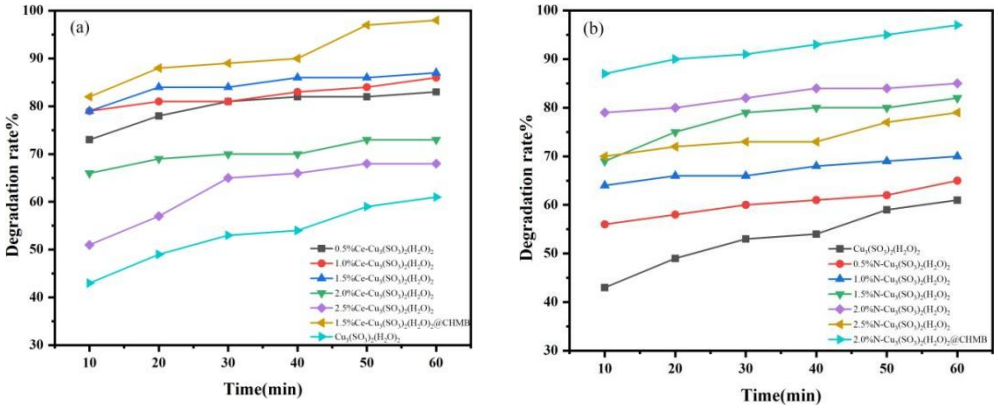



**Fig. 10**: Degradation rate diagrams of methyl orange by (a) Ce-doped and (b) N- doped $Cu_2SO_3 \cdot CuSO_3 \cdot 2H_2O$.

## 3.9 Reusability and Stability Test

Cyclic degradation experiments were performed on 1.5% Ce- $Cu_3(SO_3)_2(H_2O)_2$@CHMB, and the results are shown in Fig. 11. After four consecutive cycles, the degradation rate decreased from 98% to 82%. The decrease in catalytic activity during the cycling process is attributed mainly to the coverage of active sites by adsorbed intermediates and impurities on the catalyst surface, as well as the structural damage caused by mechanical stirring during the reaction. As revealed by the SEM characterization in Fig. 2, the CHMB support significantly improved the dispersion of $Cu_2SO_3 \cdot CuSO_3 \cdot 2H_2O$; however, a small number of active particles still detached from the support surface during prolonged cycling, thereby weakening the synergistic interaction between the support and the catalyst.

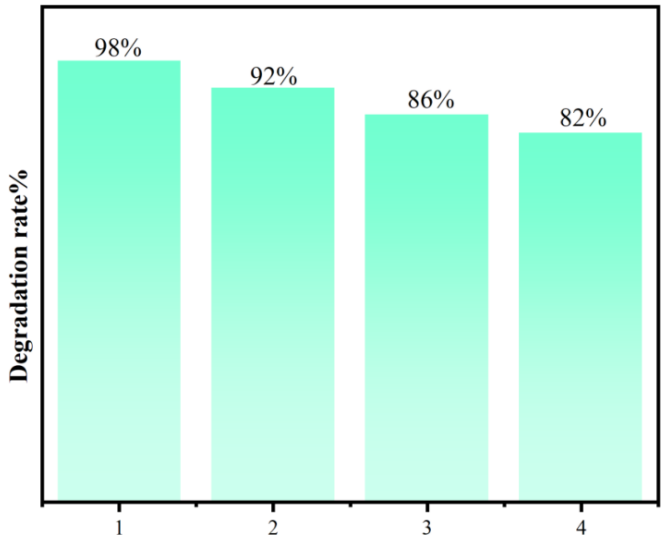



**Fig. 11**: Recycling degradation rate diagram of 1.5% Ce-doped $Cu_2SO_3 \cdot CuSO_3 \cdot 2H_2O$ @CHMB.

# 4 Conclusions:

In this study, $Cu_2SO_3 \cdot CuSO_3 \cdot 2H_2O$ was selected as the research object, and strategies involving elemental doping and support loading were adopted to investigate its structural modulation and photocatalytic performance.

**4.1** Both Ce and N doping significantly enhanced the photocatalytic activity, with optimal molar doping ratios of 1.5% and 2.0%, respectively, resulting in methyl orange degradation rates of 87% and 85%, which were markedly superior to those of the pris- tine sample. Upon further loading onto ceramic hollow microspheres, the degradation rates increased to 98% and 97%, respectively.

**4.2** SEM observations revealed that Ce doping at relatively high concentrations led to a reduction in the grain size, whereas N doping induced a flower-like clus- ter morphology. XRD and Raman analyses indicated that Ce doping decreased the crystal symmetry. UV-Vis DRS spectra revealed that both types of doping caused a significant redshift in the absorption edge, thereby extending the visible-light response range. The PL spectra confirmed that the lowest charge carrier recombination rate was achieved after loading onto the ceramic hollow microspheres. First-principles cal- culations demonstrated that Ce doping reduced the band gap from 3.464 eV to 1.660 eV, which is favorable for the separation of photogenerated electron-hole pairs.

**4.3** The degradation rate remained at 82% after four consecutive cycling experiments, indicating satisfactory photocatalytic stability of the catalyst.

# References

[1] Elgohary, E.A., et al.: A Review of the Use of Semiconductors as Catalysts in the

Photocatalytic Inactivation of Microorganisms (2021). https://doi.org/10.3390/catal11121498

[2] Wu, H., et al.: Recent advances of semiconductor photocatalysis for water pollutant treatment: mechanisms, materials and applications (2023). https://doi.org/10.1039/D3CP03391K

[3] Hoffmann, M.R., et al.: Environmental Applications of Semiconductor Photocatalysis (1995). https://doi.org/10.1021/cr00033a004

[4] Nguyen, V.-H., et al.: Photocatalytic remediation of persistent organic pollutants (POPs): A review (2020). https://doi.org/10.1016/j.arabjc.2020.04.028

[5] Hassaan, M.A., et al.: Principles of Photocatalysts and Their Different Applications: A Review (2023). https://doi.org/10.1007/s41061-023-00444-7

[6] M. Rahman, S.S., Ahmad, T.: Photocatalytic transformation of organic pollutants and remediation strategies of carbon emissions and nitrogen fixation in inland water (2025). https://doi.org/10.1016/j.mtcata.2025.100103

[7] Kumar, M., et al.: Emerging Copper-Based Semiconducting Materials for Photocathodic Applications in Solar Driven Water Splitting (2022). https://doi.org/10.3390/catal12101198

[8] Yang, Y., et al.: Recent Progress in Doped g-C3N4 Photocatalyst for Solar Water Splitting: A Review (2022). https://doi.org/10.3389/fchem.2022.955065

[9] Wang, Z., et al.: Rare Earth Doping-Regulated G-C3N4-Based Photocata- lysts: Heterojunction Construction, Mechanisms, and Synergistic Applications in Energy and Environment (2026). https://doi.org/10.1002/adsu.70458

[10] Liu, S., et al.: Modulating Electronic Structure to Improve the Solar to Hydrogen Efficiency of Cobalt Nitride with Lattice Doping (2023). https://doi.org/10.1021/acscatal.2c05075

[11] Hoffmann, M.R., et al.: Environmental Applications of Semiconductor Photocatalysis (1995). https://doi.org/10.1021/cr00033a004

[12] Duo, W.: Preparation and Properties of Novel Copper-Containing Micro-Nano Materials[D] (2013)

[13] Guan, M., et al.: Facile preparation of Chevreul's salt ($Cu_2SO_3 \cdot CuSO_3 \cdot 2H_2O$) mesocrystalline microspheres and their high photocatalytic activity (2015)

[14] Cai, J., et al.: Review on $CeO_2$-Based Photocatalysts for Photocatalytic Reduc- tion of $CO_2$: Progresses and Perspectives (2023). https://doi.org/10.1021/acs.energyfuels.3c00120

[15] Pastor, E., et al.: Electronic defects in metal oxide photocatalysts (2022). https://doi.org/10.1038/s41578-022-00433-0

[16] Asahi, R., et al.: Visible-Light Photocatalysis in Nitrogen-Doped Titanium Oxides (2001). https://doi.org/10.1126/science.1061051

[17] Valentin, D., C., G.P., Selloni, A.: Theory of Carbon Doping of Titanium Dioxide (2005). https://doi.org/10.1021/cm051921h

[18] Liu, B., Hu, X.: Liu, B. and X. Hu, Chapter 1 - Hollow Micro- and Nanomaterials: Synthesis and Applications, in Advanced Nanomaterials for Pollutant Sensing and Environmental Catalysis, Q. Zhao, Editor. 2020, Elsevier. p. 1-38. Elsevier (2020)

[19] Fang, B., et al.: Hollow semiconductor photocatalysts for solar energy conversion (2022). https://doi.org/10.1016/j.apmate.2021.11.008

[20] Dudarev S, L., Botton G, A., Savrasov S, Y., et al.: Electron-energy-loss spectra and the structural stability of nickel oxide:An LSDA+ U study (1998). https://doi.org/10.1103/PhysRevB.57.1505

**Acknowledgements**
The authors gratefully acknowledge the financial support from the Heilongjiang Provincial Department of Education through the "Double First-Class Discipline Collaborative Innovation Achievement Construction Project" (Grant No. LJGXCG2022-132).

**Funding**
This project was funded by the "Double First-Class Discipline Construction Collaborative Innovation Achievement Construction Project" of the Heilongjiang Provincial Department of Education.